Propulsion of microorganisms by a helical flagellum

Bruce Rodenborn[a], Chih-Hung Chen[a], Harry L. Swinney[a,1], Bin Liu[b], and H. P. Zhang[c,1]

[a]Department of Physics and Center for Nonlinear Dynamics, University of Texas at Austin, Austin, TX 78712; [b]School of Engineering, Brown University, Providence, RI 02912; and [c]Department of Physics and Institute of Natural Sciences, Shanghai Jiao Tong University, Shanghai 200240, China

Contributed by Harry L. Swinney, November 28, 2012 (sent for review September 16, 2012)

The swimming of a bacterium or a biomimetic nanobot driven by a rotating helical flagellum is often interpreted using the resistive force theory developed by Gray and Hancock and by Lighthill, but this theory has not been tested for a range of physically relevant parameters. We test resistive force theory in experiments on macroscopic swimmers in a fluid that is highly viscous so the Reynolds number is small compared to unity, just as for swimming microorganisms. The measurements are made for the range of helical wavelengths λ, radii R, and lengths L relevant to bacterial flagella. The experiments determine thrust, torque, and drag, thus providing a complete description of swimming driven by a rotating helix at low Reynolds number. Complementary numerical simulations are conducted using the resistive force theories, the slender body theories of Lighthill and Johnson, and the regularized Stokeslet method. The experimental results differ qualitatively and quantitatively from the predictions of resistive force theory. The difference is especially large for $\lambda < 6R$ and/or $L > 3\lambda$, parameter ranges common for bacteria. In contrast, the predictions of Stokeslet and slender body analyses agree with the laboratory measurements within the experimental uncertainty (a few percent) for all λ, R, and L. We present code implementing the slender body, regularized Stokeslet, and resistive force theories; thus readers can readily compute force, torque, and drag for any bacterium or nanobot driven by a rotating helical flagellum.

hydrodynamic interaction | motility

Gray and Hancock (1955) (1) and Lighthill (1976) (2) developed resistive force theory to describe swimming at low Reynolds number. The theory is used to interpret propulsion by a planar wave in sperm (3), small worms (4), *Chlamydomonas reinhardtii* (5), and swimmers in a granular material (6); however, rather than using the drag coefficients given by ref. 1 or ref. 2, the coefficients are usually adjusted to fit the observations. The theory is also used to describe bacterial propulsion by a rotating helical flagellum (5, 7–12) and nanobots (13–16). The algebraic expressions relating forces and torques to a helical flagellum's axial velocity and rotation rate (1, 2) are convenient to use but have not been tested for a wide range of helical parameters. The experiments reported here test resistive force theory for helical flagella. Also, we compare the laboratory observations to the predictions of slender body theory (2, 17) and regularized Stokeslet theory (18).

A helical bacterial flagellum can be modeled as a rigid rotating helix (19) with radius R, pitch λ, length L, pitch angle θ, contour length $\Lambda = L/\cos\theta$, and filament radius a (Fig. 1). The pitch is typically in the range $2R < \lambda < 11R$ and the length is in the range $3\lambda < L < 11\lambda$, as illustrated by the examples in Table 1 (10, 20–23).

For a microorganism driven by a helical flagellum rotating about its axis, the Reynolds number Re is typically $10^{-4} - 10^{-2}$, where $Re = \rho\Omega R^2/\mu$ (Ω is the rotation rate; μ, the dynamic viscosity; and ρ, the fluid density). At low Reynolds number a rotating flagellum exerts an axial thrust $\mathcal{F}$ and torque τ related to the flagellum's axial velocity U and rotation rate Ω by (24, 25)

$$\begin{pmatrix} \mathcal{F} \\ \tau \end{pmatrix} = \begin{pmatrix} A_{11} & A_{12} \\ A_{12} & A_{22} \end{pmatrix} \cdot \begin{pmatrix} U \\ \Omega \end{pmatrix}. \qquad [1]$$

The symmetric 2×2 propulsive matrix in Eq. **1** depends only on the geometry of the flagellum. The elements of the propulsive matrix can be determined by measuring the axial thrust F and torque T for a rotating nontranslating flagellum and the axial drag D on a translating nonrotating flagellum: $D = A_{11}\,U$, $F = A_{12}\,\Omega$, and $T = A_{22}\,\Omega$.

Other researchers have compared experimental measurements to resistive force theory and found that it does not accurately describe the swimming of model spirochetes (i.e., super helices) (26, 27) and swimming *Escherichia coli* (9, 28). The present work specifically examines swimming driven by a rigid helix in a Newtonian fluid (29) and compares laboratory measurements with predictions of various models for a wide range of helical parameters.

We measure thrust F, torque T, and drag D for model helical flagella that are macroscopic ($R = 6.5$ mm) but swim in a highly viscous fluid so $Re \approx 10^{-3}$. The length, pitch, and radii of the laboratory helices are varied to cover the range relevant to microorganisms and nanobots. The laboratory results are compared to the predictions of resistive force theory (1, 2) and to results from our numerical simulations of the slender body theory of Lighthill (2) and Johnson (17) and the regularized Stokeslet method of Cortez et al. (18).

Results

Comparison of Experiment and Resistive Force Theory. Our measurements of thrust, torque, and drag for flagella with different pitch are presented in Fig. 2. The results presented are dimensionless; for reference, the actual values for $\lambda = 9R$ are $F = 80$ mN, $T = 6.0$ mNm, and $D = 66$ mN. We also measured thrust, torque, and drag as a function of helix length (for fixed pitch and filament radius), as shown in Fig. 3.

The measurements in Figs. 2 and 3 depart both qualitatively and quantitatively from the resistive force theory predictions of Gray and Hancock (1) and Lighthill (2), who obtained the force and torque on a flagellum by integrating the local forces on each small segment (Fig. 1, *Inset*). Gray and Hancock's expressions for the drag coefficients in the directions normal and tangential to the segment differ from the coefficients obtained by Lighthill; both sets of expressions are given in *Methods*. For both approaches the predictions for thrust and drag differ significantly from the measurements, especially for flagella with small pitch ($\lambda < 10R$, Fig. 2) and/or large length ($L > 2\lambda$, Fig. 3). On the other hand, Lighthill's predictions for torque agree fairly well with the measurements as a function of both helix pitch (Fig. 2) and helix length (Fig. 3), whereas the Gray and Hancock predictions for torque are smaller than the measured values.

Resistive force theory fails because it neglects hydrodynamic interactions between flows induced by different parts of a flagellum; these interactions are long-ranged at low Reynolds number. As λ decreases, the separation of filament segments in a helical

Author contributions: B.R., H.L.S., and H.P.Z. designed research; B.R., C.-H.C., B.L., and H.P.Z. performed research; B.L. and H.P.Z. contributed new reagents/analytic tools; B.R., C.-H.C., H.L.S., and H.P.Z. analyzed data; and B.R., H.L.S., and H.P.Z. wrote the paper.

The authors declare no conflict of interest.

[1]To whom correspondence may be addressed. E-mail: hepeng_zhang@sjtu.edu.cn or swinney@chaos.utexas.edu.

See Author Summary on page 1574 (volume 110, number 5).

This article contains supporting information online at www.pnas.org/lookup/suppl/doi:10.1073/pnas.1219831110/-/DCSupplemental.

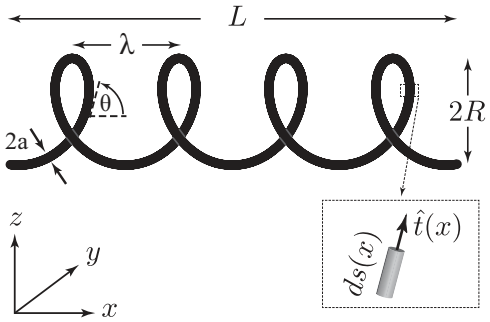

Fig. 1. Schematic of a helical flagellum with radius R, pitch λ, axial length L, filament radius a, contour length $\Lambda = L/\cos\theta$, and pitch angle θ, where $\tan\theta = 2\pi R/\lambda$. *Inset* shows a filament segment of length $ds = dx/\cos\theta$. The segment's tangential unit vector is $\hat{t}(x) = [\cos\theta, -\sin\theta\sin\phi, \sin\theta\cos\phi]$, where $\phi = 2\pi x/\lambda$ is the phase angle of the helix.

flagellum decreases, leading to stronger hydrodynamic interactions. In the limit $\lambda \to 0$, a helix becomes a cylinder that produces zero thrust. The failure of resistive force theory due to hydrodynamic interactions when helices have small pitch has been reported previously (26, 27) but not quantified. Neglect of hydrodynamic interactions also leads to the failure of resistive force theory to describe the observed length dependence shown in Fig. 3, as discussed in the next section.

Comparison of Experiment with Stokeslet and Slender Body Theories. Stokeslet and slender body theories both rely on the linearity of the Stokes equations for low Reynolds number flow. The solution at a spatial location $\mathbf{r}$ for the fluid velocity and pressure fields, $\mathbf{u}(\mathbf{r})$ and $p(\mathbf{r})$, resulting from a point force at the origin, $\mathbf{f}\delta(\mathbf{r})$, is given by a "Stokeslet" (30)

$$\mathbf{u}(\mathbf{r}) = \mathbf{f}\cdot\mathbb{J}(\mathbf{r}) \quad \text{and} \quad p(\mathbf{r}) = \frac{\mathbf{f}\cdot\mathbf{r}}{4\pi|\mathbf{r}|^3}, \qquad [2]$$

where $\mathbb{J}(\mathbf{r})$ is the Oseen tensor,

$$\mathbb{J}(\mathbf{r}) \equiv \frac{1}{8\pi\mu}\left(\frac{\mathbb{I}}{|\mathbf{r}|} + \frac{\mathbf{r}\mathbf{r}^{\mathrm{T}}}{|\mathbf{r}|^3}\right). \qquad [3]$$

The response to a continuous force distribution from an immersed body can be found by superposing Stokeslets (31). Thus, forces on a flagellum and the resultant flow field can be found by discretizing a flagellum's surface and assigning a Stokeslet to represent the fluid response to each surface element, as shown schematically in Fig. 4. The total force on the flagellum is found by integrating over the Stokeslets.

We compute the propulsive matrix elements using a technique developed by Cortez et al. (18), who used a "regularized" Stokeslet, which is an approximate point force, $\mathbf{f}\phi_\varepsilon(\mathbf{r})$, where the radial cutoff function ϕ_ε avoids singular, nonintegrable kernels in numerical simulations (*Methods*). We also compute the propulsive matrix, using the slender body theory approximation to describe flagellar swimming, as developed by Lighthill (2) and Johnson (17). Slender body theory uses Lorentz's (31) result that the far field fluid response to a moving sphere can be represented by a Stokeslet and a source dipole (doublet) of the same strength at the center of the sphere. In this approach Stokeslets and doublets are arranged along the axis of the flagellum, and the force per unit length on a flagellum is obtained by inverting the integral equation, relating the velocity of the flagellum's center line and the strength of the Stokeslets and doublets.

Numerical simulations using the regularized Stokeslet method (18) and the Lighthill (2) and Johnson (17) formulations of the slender body theory are described in *Methods*, and a Matlab version of the code (Code S1 in *SI Numerical Simulations*) can be used to reproduce the data presented in Figs. 2 and 3. As can be seen in Figs. 2 and 3, the results from both slender body theory

Table 1. Parameters of flagella for several species of bacteria [the filament radius a is typically 0.01 μm (20)]

Organism (ref.)	R, μm	λ/R	L/λ
Caulobacter crescentus (21)			
Wild type	0.13	8.3	6
Escherichia coli (10)			
CCW	0.195 ± 0.025	11	2.8
Stopped	0.210 ± 0.025	11	2.7
Rhizobium lupini (22)			
Normal	0.250 ± 0.015	5.4	4
Semicoiled	0.385 ± 0.020	2.9	3
Curly	0.135 ± 0.020	9.4	5
Salmonella (23)			
Wild type	0.210 ± 0.005	11	4
Curly mutant	—	—	11
Tumbling mutant	0.145 ± 0.005	7.6	9

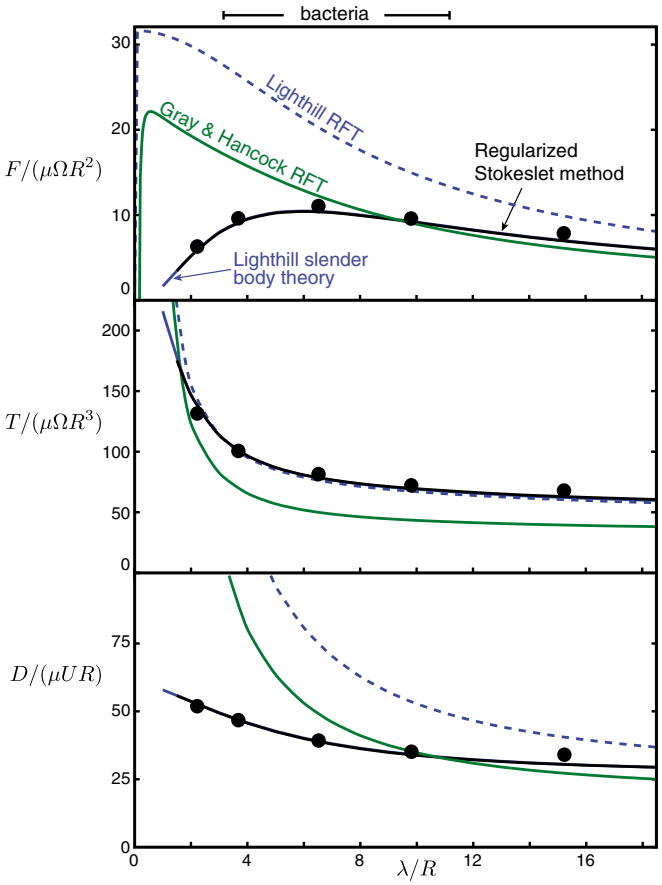

Fig. 2. Thrust, torque, and drag for helical flagella as a function of pitch λ (relative to the helix radius R) for helix length $L = 20R$ and filament radius $a = R/16$: experiment (solid black circles), regularized Stokeslet theory (solid black lines), slender body theory of Lighthill (2) (solid blue lines), resistive force theory of Gray and Hancock (1) (green lines), and resistive force theory of Lighthill (2) (dashed blue lines). The regularized Stokeslet theory and slender body theory results are very similar so the curves can be difficult to distinguish; results from the slender body theory of Johnson (17) are essentially the same and so are not plotted.

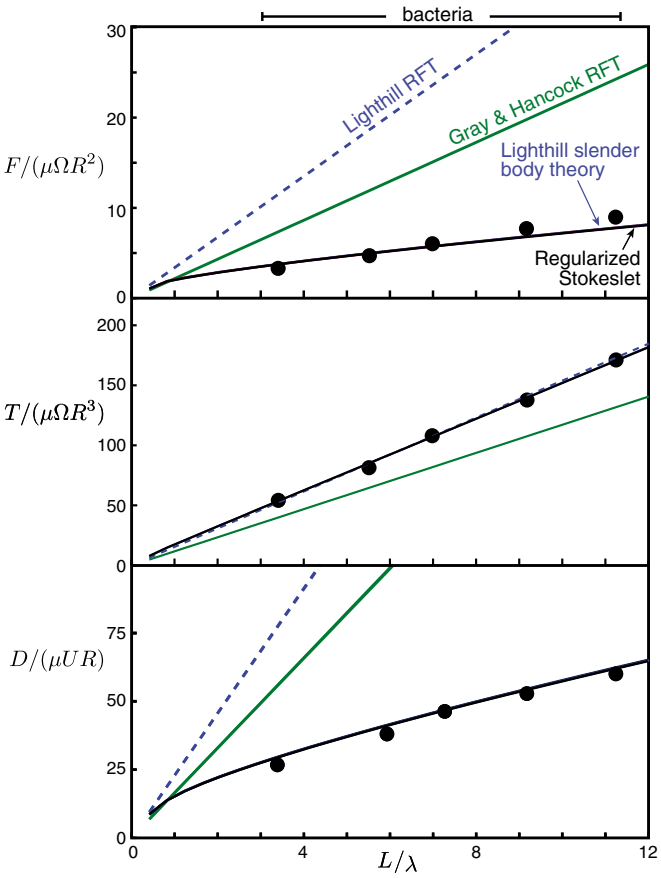

Fig. 3. Thrust, torque, and drag for helical flagella as a function of length for flagella with the same filament radius $a = R/16$ and pitch $\lambda = 2.42R$: experiment (solid black circles), regularized Stokeslet theory (solid black lines), slender body theory of Lighthill (2) (solid blue lines), resistive force theory of Gray and Hancock (1) (green lines), and resistive force theory of Lighthill (2) (dashed blue lines). The regularized Stokeslet theory and slender body theory results are very similar so the curves can be difficult to distinguish; results from the slender body theory of Johnson (17) are essentially the same and so are not plotted.

and the regularized Stokelets method agree well with the laboratory observations; the difference is within the experimental uncertainty. The good agreement between measurements and calculations for the flagella suggests that the stationary motor housing, unlike with a moving cell body (9), does not interact strongly with the flagellum.

Long Flagella. By expanding Lighthill's slender body expressions (*Methods*), we obtain scaling relationships for thrust, torque, and drag in the limit $L \to \infty$,

$$F = -\left(\frac{a_2}{a_1 a_4}\right)\frac{L}{\ln(L/R)}\Omega \quad [4]$$

$$T = \left(\frac{1}{a_4}\right)L\Omega \quad [5]$$

$$D = \left(\frac{1}{a_1}\right)\frac{L}{\ln(L/R)}U, \quad [6]$$

where the constants a_1–a_4 depend on the flagellum geometry (expressions are given in *Methods*).

The logarithmic factor in the expressions for thrust and drag in the long length limit is absent in resistive force theory, but is necessary to obtain the length dependence behavior we found. The predictions of the asymptotic analysis agree within a few percent with both the Lighthill and Johnson versions of slender body theory for $L/\lambda > 1{,}000$ ($\lambda = 2.42R$). In the limit $L \to \infty$, slender body theory and resistive force theory predict the same functional dependence, but the proportionality coefficient for resistive force theory is different from that for slender body theory. Further, our thrust and drag data in the biologically relevant regime $L/R < 30$ are consistent with $L/\ln(L/R)$ scaling within the experimental uncertainty.

Dependence on Filament Radius. We use the slender body theory and regularized Stokeslet method simulations to examine the dependence of force, torque, and drag on filament radius, which was fixed in our experiments at $a/R = 0.063$. The filament radius results from slender body theory and the regularized Stokeslet method agree well for radii relevant to bacterial filaments ($a/R < 0.07$), as shown in Fig. 5. For larger a/R values, not relevant to bacteria but possibly relevant to some nanobots, the Stokeslet simulations predict torque values somewhat larger than predicted by slender body theory. The results in Fig. 5, like those in Figs. 2 and 3, can be generated using code provided as Code S1 in *SI Numerical Simulations*.

Discussion

Our experiments reveal that resistive force theory fails to provide an accurate description of low Reynolds number swimmers driven by a rotating helical flagellum for helices with $\lambda < 6R$ and/or $L > 3\lambda$, which is the range relevant to bacteria. The measured values of thrust, torque, and drag differ significantly from the predictions of resistive force theory with either Gray and Hancock's (1) or Lighthill's (2) drag coefficients (Figs. 2 and 3). The measurements were made for values of helical pitch λ and length L that include the ranges relevant to bacteria.

Hancock (30) pioneered the analysis of swimming microorganisms more than a half century ago. His "slender body model" yielded predictions in terms of integrals that could not be nu-

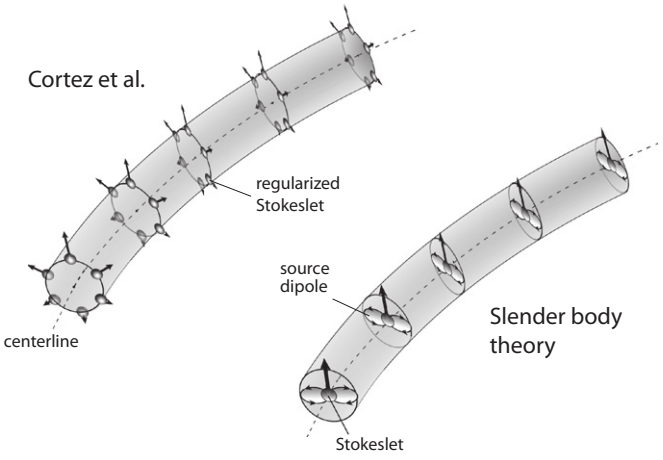

Fig. 4. Regularized Stokeslet method of Cortez et al. (18) discretizes the surface of the flagellum and represents each surface element by a regularized Stokeslet, which approximates a Stokeslet but avoids using delta function singularities. Slender body theory represents a flagellum using Stokeslets and doublets arranged along the helical centerline; the combination of a Stokeslet plus dipole approximates the fluid response to a flagellum segment. In the simulations, the distance between cross sections is smaller than their separation in the drawing, and there are 12 regularized Stokeslets per cross section rather than 6 as drawn (*Methods*).

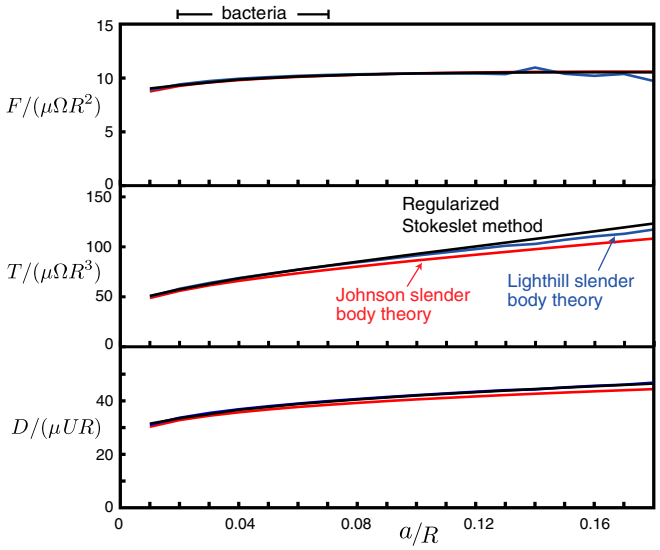

Fig. 5. Thrust, torque, and drag of flagella as a function of filament radius a relative to the helical radius R (for a helix with pitch $\lambda = 6R$ and length $L = 20R$). The black curves are calculations using the regularized Stokeslet method, the blue curves are Lighthill slender body theory calculations, and the red curves are Johnson slender body theory calculations. The values calculated for thrust from slender body theory curves cannot be distinguished from the Stokeslet theory curves. We do not include here results from resistive force theory because they are mostly off the scale of this graph.

merically evaluated at that time. Then Gray and Hancock (1) developed "resistive force theory," which yielded expressions for thrust, torque, and drag in terms of the normal and tangential resistance coefficients.

Resistive force theory was subsequently reanalyzed by Lighthill (2). He computed zero-thrust free swimming speed (equation 57 in his paper) for "an infinitely long flagellum" from his slender body theory. He then used this computed zero-thrust swimming speed and expressions for the force distribution as "experimental data" to calibrate resistive force theory and got "improved" expressions for drag coefficients. Thus one can use Lighthill's resistive force theory coefficients to predict the free speed for a helical flagellum without a cell body, but the theory fails when the cell body produces significant drag (nonzero thrust) (28).

The primary advantage of resistive force theory has been its computational simplicity; the results are given in terms of algebraic expressions without the necessity of numerical integration. But numerical integration is now straightforward on desktop computers. We have developed numerical implementations of regularized Stokeslet theory and two versions of slender body theory, which were used to produce the curves in Figs. 2, 3, and 5. These algorithms (Code S1 in *SI Numerical Simulations*) can be used by a reader to compute thrust, torque, and drag for any rotating helix with parameters R, λ, L, and a.

In conclusion, we have shown that slender body theory and regularized Stokeslet theory predictions are in good accord with measurements on low Reynolds number swimmers driven by a rotating helix. This work indicates that it should also be straightforward to apply slender body theory to microscopic undulating swimmers, whose motion is often interpreted using resistive force theory (3–6).

Methods

System. Experiments were performed in an 80-L tank (520 mm × 495 mm × 330 mm high) filled with silicone oil (Clearco) of density 970 kg/m^3 and dynamic viscosity (at 25 °C) $\mu = 1.0 \times 10^2$ kg·m^{-1}·s^{-1}), about 10^5 times that of water. We measured the viscosity of the silicone oil with a cone and plate viscometer and obtained a value in agreement with that given by the manufacturer; we used the manufacturer's values for the temperature coefficient of viscosity, 1.00×10^{-6} kg·m^{-1}·s^{-1}/°C and thermal expansion coefficient, 9.4×10^{-4}/°C. We measured the oil temperature using a calibrated thermistor (Barnant Model 600-1075 LogR Thermistor/Datalogger).

Model flagella were constructed from initially straight pieces of type 304 stainless steel welding wire with radius 0.397 mm. The wire was wrapped around aluminum mandrels with helical V-shaped grooves of varying pitches on rods with radius 6.4 mm and lengths of either 152.5 or 305 mm. In measurements of the dependence on pitch, the helical radius was $R = 6.3 \pm 0.4$ mm, the length was $L = 130 \pm 5$ mm, and pitch was varied in the range $2.2R < \lambda < 15.3R$. In measurements of the dependence on length, the radius was $R = 6.6 \pm 0.2$ mm, the pitch was $\lambda = 2.42R \pm 0.02R$, and the length was varied in the range $3.3\lambda < L < 11.2\lambda$. Measurements were made with each flagellum's axis about 250 mm from the tank walls to minimize boundary effects. The ends of a flagellum were kept at least 100 mm from the wall boundaries and from the free surface. To examine possible changes of the radius and wavelength of the wire helices under load, we analyzed videos for different rotation rates and for different rotation directions, and the change in wavelength and radius was smaller than the measurement uncertainty.

Thrust Measurements. A block of acrylic (89 mm × 38 mm × 35 mm) housed a reversible variable-speed motor (Pololu 298:1 Micro Metal Gear Motor) that rotated a flagellum immersed in the silicone oil (Fig. 6*A*). A stainless steel shaft adapter extended through the bearing, connecting the motor shaft inside the body to the flagellum outside of the body.

To measure the thrust generated by a rotating flagellum, the swimmer was attached to a load cell (Omega LCL-227G), using a 9.5-mm diameter vertical rod extending from a structure above the tank. This vertical rod was fitted into two ball bearings (VXB R6 3/8″ × 7/8″ × 7/32″ Full Ceramic Miniature Ball Bearing) to constrain the swimmer's movement to one direction. The distance from the bearings' center of rotation to the center of an attached flagellum was 325 mm. The load cell was at the top of the vertical rod, 25.4 mm above the bearings' center of rotation. With this arrangement, the force acting on the load cell is about 10 times larger than generated thrust, thereby increasing the measurement sensitivity. The load cell had a maximum deflection of 1.27 mm for a full-scale load (2.23 N); therefore the swimmer could rotate at most 3° at the bottom end of the vertical rod.

The load cell was connected to an amplifier/driver (Omega DP25B-E-A 1/8 DIN Process Meter and Controller) and its output fed into a digital data acquisition board (National Instruments NIDAQ 6008 USB) that also provided motor speed control (Pololu TReX Jr Dual Motor Controller DMC02A). We recorded videos of the flagellum during each 200-s–long recording of load cell data. Flagellum rotation rates were determined by analyzing the movie with a Matlab Power Spectral Density function. The composite spectrum produced by averaging the 10^3 spectra from the region of the image containing the flagellum had a peak (more than three orders of magnitude above the noise level) corresponding to the flagellum rotation rate (~0.50 Hz). For each flagellum, we measured the force for clockwise (CW) and counterclockwise (CCW) rotation for six or seven rotation speeds in each direction; the results from CW and CCW rotation differed typically by 2%. We fitted the data for each rotation direction to a line, and the average slope of these two lines yielded the force per unit frequency for the flagellum (Fig. 7*A*).

Torque Measurements. The torque required to rotate a flagellum was measured with a torque sensor (Magnova MLY Torque Transducer, maximum torque, ±25 mNm; manufacturer's stated accuracy, ±1% of full scale). For torque measurements, the flagellum was mounted to a straight vertical rod using the 6.35-mm diameter adapter (Fig. 6*B*). The stepper motor used to rotate the flagellum gave precise control of rotation rate so no frequency analysis was required. Again, multiple measurements at different rotation speeds were made and fit to a line, giving the torque per unit frequency in each direction; these values were averaged. There is also a background offset in this measurement. The torque created by rotating the rod and adapter alone was subtracted from the value measured when a flagellum was attached. Fig. 7*B* shows that the background value for these data was about 30% of the total signal; the final torque value has an uncertainty of 4%.

Drag Measurements. The drag on a flagellum was measured by translating the nonrotating flagellum horizontally, as illustrated in Fig. 6*C*. The flagellum was mounted on a 9.5-mm diameter vertical rod that had a 6.35-mm diameter adapter mounted perpendicular to the vertical rod into which the flagellum was mounted. The rod, shaft adapter, and flagellum assembly were pulled through the fluid for 70 mm, and the drag was measured with the same load cell as for thrust measurements. Six or seven measurements were made at different translation velocities in both the flagellum-first and

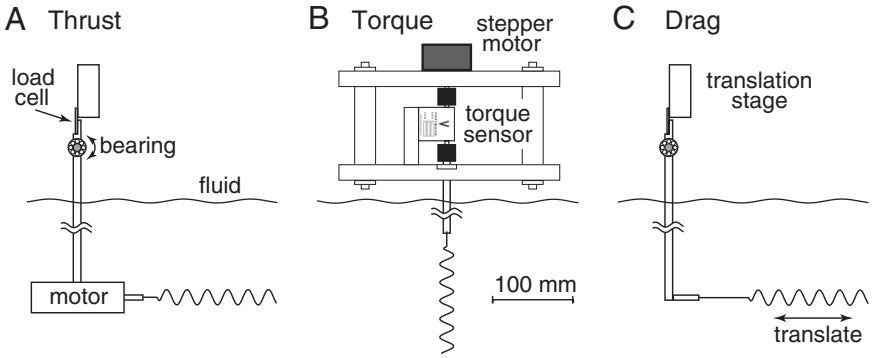

Fig. 6. Schematic drawings of measurements of (*A*) thrust, (*B*) torque, and (*C*) drag.

the rod-first directions. Data for each direction were fitted to a line with the average of the two slopes giving the final drag force per unit velocity. This result included the drag from the rod and adapter, which was independently measured (for motion in both directions) and subtracted from the force measured with the flagellum attached (Fig. 7*C*). The background was typically 80% of the total signal, but the uncertainty in the flagellum drag was still less than 3%.

Experimental Data. Fig. 7 shows typical data used to determine thrust, torque, and drag. The data are linear with respect to the rotation rate or velocity, depending on the measurement. Despite large background values for the rod and adapter holding the flagellum, the values of torque and drag determined from the linear fit have uncertainties typically less than 5%.

Numerical Simulations

A program titled Helical Swimming Simulator, provided here as Code S1 in *SI Numerical Simulations*, calculates thrust, torque, and drag for any helical flagellum, using the regularized Stokeslet method, Lighthill's formulation of slender body theory, or Johnson's version of slender body theory; resistive force theory results are also provided for comparison. (To permit updates, the code, entitled "Helical Swimming Simulator," is also provided on the Matlab File Exchange, www.mathworks.com/matlabcentral/fileexchange/.) The program takes as input the parameters for a helical flagellum: radius R, pitch λ, length L, filament radius a, velocity U, and rotation rate Ω. The helical radius R is used as the unit of length; thrust, torque, and drag are made dimensionless by dividing by $\mu\Omega R^2$, $\mu\Omega R^3$, and μUR, respectively. The following describes the methods used for each type of calculation.

Resistive Force Theory. Resistive force theory obtains the total force and torque for motion of a flagellum by integrating the local forces on each small segment (Fig. 1, *Inset*). The local forces are calculated using drag coefficients per unit length in the directions normal and tangential to the segment, C_n and C_t, respectively. Resistive force theory predicts that the thrust, torque, and drag on a flagellum are given by

$$F = (\Omega R)(C_n - C_t)\sin\theta\cos\theta\frac{L}{\cos\theta}, \quad [7]$$

$$T = (\Omega R^2)\left(C_n\cos^2\theta + C_t\sin^2\theta\right)\frac{L}{\cos\theta}, \quad [8]$$

$$D = U\left(C_n\sin^2\theta + C_t\cos^2\theta\right)\frac{L}{\cos\theta}. \quad [9]$$

Two sets of drag coefficients are commonly used in the literature, those by Gray and Hancock (1) and those by Lighthill (2); both are based on slender body theory, assuming that the effect of each small filament segment is only locally important. Gray and Hancock's drag coefficients are

$$C_t = \frac{2\pi\mu}{\ln\frac{2\lambda}{a} - 1/2} \quad \text{and} \quad C_n = \frac{4\pi\mu}{\ln\frac{2\lambda}{a} + 1/2} \quad [10]$$

and Lighthill's are

$$C_t = \frac{2\pi\mu}{\ln\frac{0.18\lambda}{a\cos\theta}} \quad \text{and} \quad C_n = \frac{4\pi\mu}{\ln\frac{0.18\lambda}{a\cos\theta} + 1/2}. \quad [11]$$

These drag coefficients are used in Eqs. **7–9** for comparison with experiments. See Figs. 2 and 3.

Regularized Stokeslet Method. Stokeslet theory includes Dirac delta functions, which are difficult to evaluate computationally. Therefore, Cortez et al. (18) use an approximate delta function, a radially symmetric cutoff function $\phi_\varepsilon(\mathbf{r})$ given by

$$\phi_\varepsilon(\mathbf{r}) = \frac{15\varepsilon^4}{8\pi(r^2+\varepsilon^2)^{7/2}}, \quad [12]$$

where $r = |\mathbf{r}|$ and ε is assumed to be small. This regularization parameter prevents nonintegrable kernels, but also has a physical meaning representing surface area over which the force is distributed. Over 97% of the weight of Eq. **12** is within a radius of one ε.

For N regularized point forces $\mathbf{f}\phi_\varepsilon(\mathbf{r}_n)$ at locations $\mathbf{r}_n$ on the surface of a body in motion, the fluid velocity at any point $\mathbf{r}$ is

$$u_j(\mathbf{r}) = \frac{1}{8\pi\mu}\sum_{n=1}^{N}\sum_{i=1}^{3} S_{ij}^{\varepsilon}(\mathbf{r}-\mathbf{r}_n)f_{n,i}A_n, \quad [13]$$

where A_n are quadrature weights, and the regularized Green's function S_{ij}^{ε} is

$$S_{ij}^{\varepsilon}(\mathbf{r}) = \frac{\delta_{ij}(r^2+2\varepsilon^2) + r_i r_j}{(r^2+\varepsilon^2)^{3/2}}. \quad [14]$$

The regularized Green's function S_{ij}^{ε} depends only on the geometry of the object in motion and the regularization parameter ε. Evaluating Eq. **13** at each of the N regularized Stokeslets gives a linear relation between the velocities and the forces exerted at these points.

For a helical flagellum, we discretize the surface with cross sections along its length and use 12 regularized Stokeslets on the perimeter of each circular cross section. We separate adjacent cross sections by a distance equal to one-half of the filament

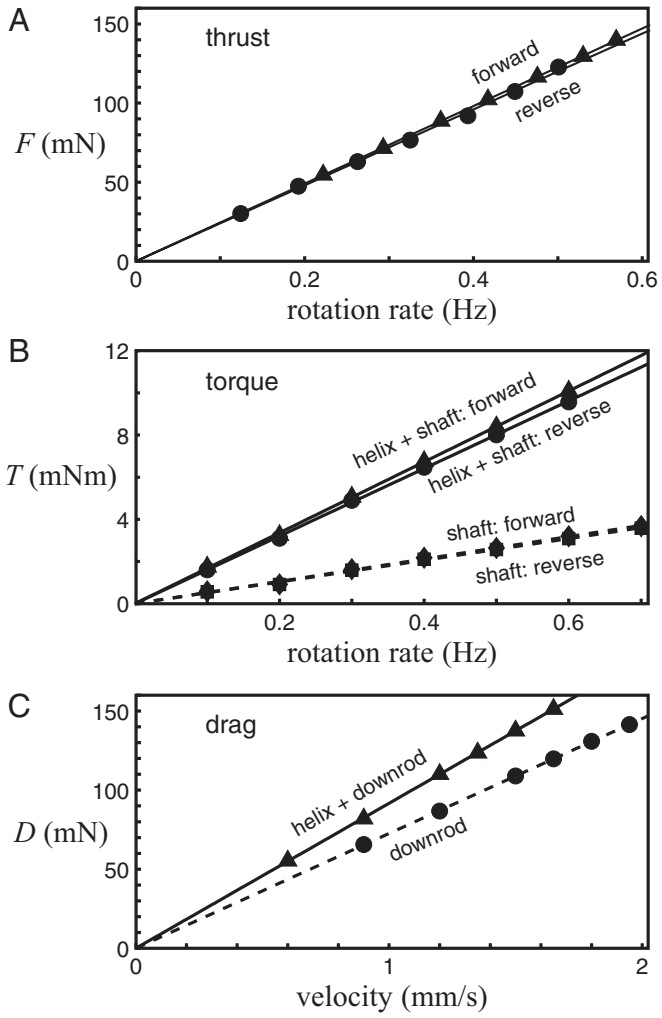

Fig. 7. (*A*) Thrust measurements for a flagellum with $R = 6.6$ mm, $a = R/16$, $L = 20R$, $\lambda = 6.5R$: slope for forward rotation = 245.3 ± 0.8 mN/Hz; slope for reverse rotation = 239.9 ± 5.4 mN/Hz; average slope = 242.6 ± 5.5 mN/Hz (2.3% uncertainty). (*B*) Torque measurements: slope for helix + shaft = 16.8 ± 0.2 mNm/Hz; reverse slope = 16.0 ± 0.2 mNm/Hz; average slope = 16.4 ± 0.3 mNm/Hz; slope for shaft alone = 5.3 ± 0.2 mNm/Hz; reverse slope = 5.1 ± 0.1 mNm/Hz; average = 5.2 ± 0.2 mNm/Hz. The resultant net torque is 11.2 ± 0.4 mNm/Hz (3.6% uncertainty). (*C*) Drag measurements: slope for helix + downrod = 91.6 ± 0.4 $N{\cdot}s^{-1}{\cdot}m^{-1}$; slope for downrod alone = 272.6 ± 0.3 $N{\cdot}s^{-1}{\cdot}m^{-1}$. The difference is the net torque = 19.0 ± 0.5 $N{\cdot}s^{-1}{\cdot}m^{-1}$ (2.6% uncertainty).

radius. We choose a regularization parameter ε to be half of the grid spacing so adjacent regularized Stokeslets do not overlap extensively. Fig. 8 shows the effect of varying ε and varying grid spacing in simulations of thrust, torque, and drag for a flagellum similar to those in the experiments. Using a value of $\varepsilon/\Delta s = 1/2$, we obtain values for F, T, and D that are nearly the same for all three grid resolutions. Increasing the grid resolution from $\Delta s = a/2$ to $\Delta s = a/3$ changes the values by less than 1%, providing $\varepsilon/\Delta s = 1/2$. However, the values change by about 1.5% for a 20% change in ε.

Because the regularized Stokeslet method results depend on the choice of ε, we also simulated flagellar propulsion, using a new boundary integral method developed by Gonzalez (32) for solving solid body Stokes flow problems. This numerical method also discretizes the flagellum surface and assigns Stokeslets to represent each surface element, and it includes a parallel offset parameter, which is the distance by which a parallel virtual surface is offset from the flagellum. The flow is solved using a single-layer potential on the parallel surface and a related double-layer potential on the flagellum. The two potentials have a unique solution that depends on the no-slip boundary condition of the flagellum. The solution gives the strength of the Stokeslets at the surface and thus the fluid stresses on the flagellum. The advantage of this formulation is that Gonzalez shows the results are independent of the choice of parallel offset parameter and so its choice is based on ease of solvability (32, 33).

We solved Eq. **13** numerically for point forces f_j for boundary conditions specified by u_i. Using the computed f_j, we determined the dependence of the thrust, torque, and drag on wavelength, length, and filament radius, using the methods of both Cortez et al. (18) and Gonzalez (32) with the same grid resolution in both studies, $\Delta s = a/2$ (i.e., 12 Stokeslets per cross section). There was less than 0.5% difference between the two methods providing $\varepsilon/\Delta s = 1/2$ in the regularized Stokeslet simulations. This close correspondence provides further support for our choice of ε. Other recent studies such as ref. 34 used $\varepsilon/\Delta s = 7/12$ because it gave results very similar to slender body theory calculations, whereas ref. 35 used $\varepsilon/\Delta s = 1/3$ because it seemed to give the best convergence as a function of grid spacing to the analytic solution for the flow past an ellipsoid. We find that for our geometry $\varepsilon/\Delta s = 1/2$ gives results that are the most similar to both slender body theory and to the Gonzalez method, as well as to the experimental data.

Lighthill Slender Body Theory. Slender body theory represents a flagellum with an arrangement of Stokeslets and doublets along the flagellum's centerline. Because dipolar fields fall off as r^{-2},

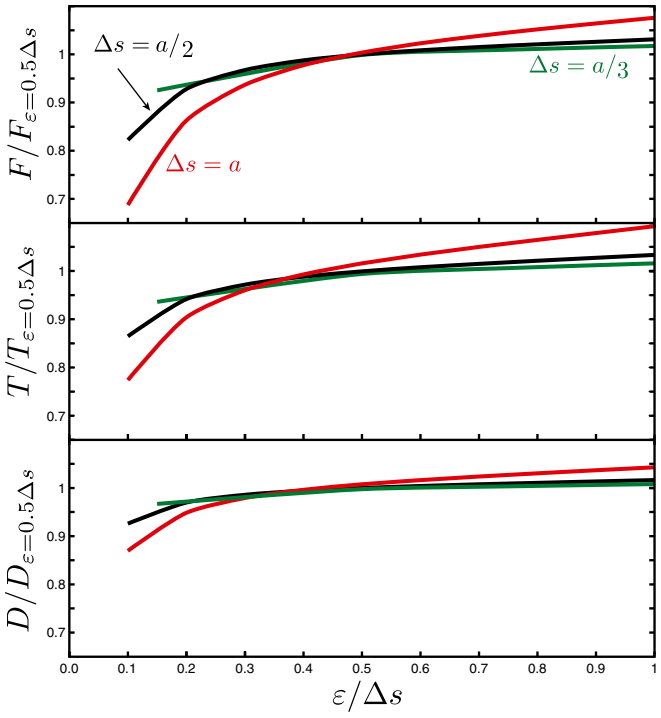

Fig. 8. Thrust, torque, and drag from regularized Stokeslet method simulations using different values of the regularization parameter ε and for different grid resolution for a helix with pitch $\lambda = 6R$, length $L = 20R$, and $a/R = 1/16$. Data are scaled by the value with $\varepsilon/\Delta s = 1/2$ and $\Delta s = a/2$ (12 regularized Stokeslets per cross section), the values used in our analysis. The red curves are simulations using $\Delta s = a$ (6 regularized Stokeslets per cross section), and the green curves are results from simulations with $\Delta s = a/3$ (18 regularized Stokeslets per cross section). Different wavelengths have similar dependence on ε; thrust is more sensitive to its variation. However, near $\varepsilon = \Delta s/2$ the values change slowly when ε is either increased or decreased.

whereas Stokeslets fall off as r^{-1}, Lighthill (2) reasoned there should be some intermediate distance q from any given point on the flagellum where only dipoles within $a \ll q \ll \lambda$ are important in determining the flow at that point, although all of the Stokeslets on the centerline must be considered because they are longer ranged. He showed that the sum of the near- and far-field solutions for the induced fluid flow on a given segment could be made independent of q by the choice of dipoles of the form (36, 37)

$$-\frac{a^2\mathbf{f}_\perp(s)}{4\mu}, \qquad [15]$$

where $\mathbf{f}_\perp(s)$ is the component of the Stokeslet strength $\mathbf{f}$ in the plane perpendicular to the flagellum's centerline at a location s along the centerline of the flagellum (2). This combination of a Stokeslet plus a dipole determines the flow induced by each element of the flagellum. Lighthill showed that the local velocity of a segment of the helix located at s is related to the force per unit length (i.e., Stokeslet strength) along the filament $\mathbf{f}(s)$ by

$$\mathbf{u}(s) = \frac{\mathbf{f}_\perp(s)}{4\pi\mu} + \int\limits_{|\mathbf{r_0}(s',s)|>\delta} \mathbf{f}(s')\cdot\mathbb{J}(\mathbf{r_0})ds', \qquad [16]$$

where $\delta = a\sqrt{e}/2$ is the "natural cutoff" (2), r_0 is the position vector from the point s on the centerline relative to the point s', and $\mathbb{J}$ is given by Eq. **3**.

We evaluate Eq. **16** using the rectangular rule of numerical integration to calculate the thrust, torque, and drag for flagella with the same parameters as in the experiments. Our numerical scheme, similar to the method used in ref. 29, uses the helical phase $\varphi \equiv ks\cos\theta$, where $k = 2\pi/\lambda$, to parameterize spatial locations

$$\mathbf{r}(\varphi) = R(\varphi\cot\theta, \cos\varphi, \sin\varphi), \qquad [17]$$

so Eq. **16** becomes

$$\mathbf{u}_n = \frac{(\mathbb{I}-\hat{t}_n\hat{t}_n + D_n)\cdot\mathbf{f}_n}{4\pi\mu} + \frac{R\Delta\varphi\,\csc\theta}{8\pi\mu}\sum_{m\neq n}\frac{\mathbb{I}+\hat{r}_{nm}\hat{r}_{nm}}{r_{nm}}\cdot\mathbf{f}_m + \mathscr{O}(\Delta\varphi), \qquad [18]$$

where $n, m = 1, 2, \ldots, N$, $\mathbf{r}_{nm} = \mathbf{r}(\varphi_n) - \mathbf{r}(\varphi_m)$ is the position vector between spatial locations, $\hat{t}_n = (\cos\theta, -\sin\theta\sin\varphi_n, \sin\theta\cos\varphi_n)$ is the tangential unit vector at $\mathbf{r}_n$, and $\Delta\varphi$ is the mesh size of the helical phase. Note that the integral in Eq. **16** is separated into two terms in Eq. **18**. The first part of the integral is represented by the tensor D_n, which is the integral from the lower bound (natural cutoff) to the size of the grid spacing. D_n is solved explicitly because this portion of the integral is below the grid resolution and would otherwise be unresolved. The remainder of the integral appears as the second term in Eq. **18**.

We now work in a frame rotated with the helical phase to derive expressions for the velocity components $\mathbf{u}_n$ that are invariant along the helix. We use these invariant velocity components to create a linear mapping between the velocity and force per unit length, which can be evaluated for a specified helical geometry, helical axial velocity U, and rotation rate Ω to give the thrust, torque, and drag.

The tensor D_n is symmetric and is the contribution of the helical segment centered at $\mathbf{r}$, located at a distance between the cutoff length δ and the grid size away from $\mathbf{r}_n$; i.e., $|\mathbf{r}-\mathbf{r}_n| \in (\delta, \delta')$, where

$$\delta' = \frac{1}{2}R\Delta\varphi\,\csc\theta \qquad [19]$$

and D_n is the expansion of the following integral to the lowest order of the grid size $\Delta\varphi$,

$$D_n = \frac{1}{2}\int\limits_{|\mathbf{r}-\mathbf{r}_n|\in(\delta,\delta')} \mathrm{d}s(\varphi)\left(\frac{\mathbb{I}}{|\mathbf{r}-\mathbf{r}_n|} + \frac{(\mathbf{r}-\mathbf{r}_n)(\mathbf{r}-\mathbf{r}_n)}{|\mathbf{r}-\mathbf{r}_n|^3}\right)\cdot\mathscr{R}_z(\varphi-\varphi_n), \qquad [20]$$

where $\mathscr{R}_z$, the rotation operator along the axial direction, can be expressed as

$$\mathscr{R}_z(\varphi) = \begin{pmatrix}\cos\varphi & -\sin\varphi & 0\\ \sin\varphi & \cos\varphi & 0\\ 0 & 0 & 1\end{pmatrix}. \qquad [21]$$

For simplicity, we introduce new velocity and force density vectors as

$$\mathbf{u}'_n = \mathscr{R}_z(-\varphi_n)\cdot\mathbf{u}, \quad \mathbf{f}'_n = \mathscr{R}_z(-\varphi_n)\cdot\mathbf{f}_n \qquad [22]$$

so that $\mathbf{u}'_n$ is invariant along the helical filament. For a rigid helix that rotates at rate Ω and translates at speed U along its axial direction, we have

$$\mathbf{u}'_n = (0, \Omega R, U)^T \qquad [23]$$

and

$$\sum_n \mathbf{f}'_n R\Delta\varphi\,\csc\theta = \left(0, \frac{T}{R}, F_x\right)^T. \qquad [24]$$

Lighthill's slender body theory can thus be formulated as

$$\mathbf{u}'_n = \frac{(\mathbb{I}-\hat{t}'\hat{t}' + D'_n)\cdot\mathbf{f}'_n}{4\pi\mu} + \frac{R\Delta\varphi\,\csc\theta}{8\pi\mu}\sum_{m\neq n}\frac{\mathscr{R}_z(\varphi_m-\varphi_n) + \mathscr{R}_z(-\varphi_n)\cdot\hat{r}_{nm}\hat{r}_{nm}\cdot\mathscr{R}_z(-\varphi_n)}{r_{nm}}\cdot\mathbf{f}'_m + \mathscr{O}(\Delta\varphi), \qquad [25]$$

where $\hat{t}'$, D'_n are now invariant along the helical filament,

$$\hat{t}' = (0, \sin\theta, \cos\theta) \qquad [26]$$

and

$$D'_n = \int\limits_{k\delta\cos\theta}^{k\delta'\cos\theta}\mathrm{d}\varphi\frac{1}{\varphi}\left[\mathbb{I} + \begin{pmatrix}0 & 0 & 0\\ 0 & \sin^2\theta & \sin\theta\cos\theta\\ 0 & \sin\theta\cos\theta & \cos^2\theta\end{pmatrix}\right] = \ln\left(\frac{\delta'}{\delta}\right)(\mathbb{I}+\hat{t}'\hat{t}'). \qquad [27]$$

Therefore, the linear mapping between the velocity $\mathbf{u}'$ and force density $\mathbf{f}'$ is given by

$$\begin{pmatrix}\mathbf{u}'_1\\ \mathbf{u}'_2\\ \cdots\\ \mathbf{u}'_N\end{pmatrix} = \mathscr{G}\cdot\begin{pmatrix}\mathbf{f}'_1\\ \mathbf{f}'_2\\ \cdots\\ \mathbf{f}'_N\end{pmatrix}. \qquad [28]$$

For prescribed motion of a rigid helix, e.g., $\mathbf{u}'_n = \mathbf{u}_0 = (0, \Omega R, U)^T$, we have

$$\begin{pmatrix} \mathbf{f}'_1 \\ \mathbf{f}'_2 \\ \cdots \\ \mathbf{f}'_N \end{pmatrix} = \mathscr{G}^{-1} \cdot \begin{pmatrix} \mathbf{u}_0 \\ \mathbf{u}_0 \\ \cdots \\ \mathbf{u}_0 \end{pmatrix}. \quad [29]$$

The net axial hydrodynamic force F_x and the net torque T are thus given by

$$\left(0, \frac{T}{R}, F_x\right)^T = \sum_{i=1}^{N} \mathbf{f}'_n R \Delta\varphi \csc\theta, \quad [30]$$

allowing us to calculate the thrust, torque, and drag for any helical flagellum.

Johnson Slender Body Theory. Johnson (17) created a formulation of slender body theory to model the end effects ignored by Lighthill. The primary difference between the two formulations is that Johnson's slender body is a long slender prolate spheroid that terminates smoothly. Johnson's slender body theory gives the following equations for the velocity of a point on a helical flagellum in terms of local and nonlocal velocity terms,

$$\mathbf{u}(\mathrm{r}) = \mathbf{u}_{\mathrm{local}}(\mathbf{r}) + \mathbf{u}_{\mathrm{nonlocal}}(\mathbf{r}) \quad [31]$$

with

$$\mathbf{u}_{\mathrm{local}}(\mathrm{r}) = \frac{1}{8\pi\mu}\left[-\ln\left(\kappa^2 \mathrm{e}\right)\left(\mathbb{I} + \hat{t}(\mathbf{r})\hat{t}(\mathbf{r})\right) + 2\left(\mathbb{I} - \hat{t}(\mathbf{r})\hat{t}(\mathbf{r})\right)\right] \cdot \mathbf{f}(0), \quad [32]$$

and

$$\mathbf{u}_{\mathrm{nonlocal}}(\mathbf{r}) = \int \mathbb{J}\left(\mathbf{r}' - \mathbf{r}\right) \cdot \mathbf{f}\left(\mathbf{r}'\right) \mathrm{d}\mathbf{r}' - \frac{1}{8\pi\mu} \int \frac{\mathbb{I} + \hat{t}\left(\mathbf{r}'\right)\hat{t}\left(\mathbf{r}'\right)}{|s - s'|} \cdot \mathbf{f}\left(\mathbf{r}'\right) \mathrm{d}\mathbf{r}', \quad [33]$$

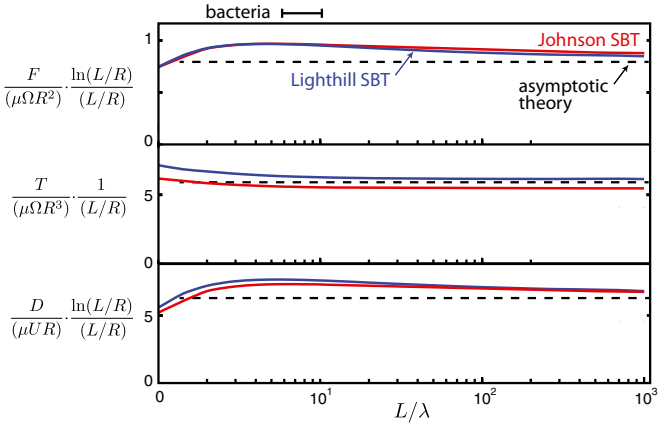

Fig. 9. Thrust, torque, and drag from slender body theory calculations are rescaled and plotted as functions of axial length L. The solid blue curves are the results of calculations for Lighthill slender body theory, the solid red curves are from Johnson slender body theory calculations, and the dashed lines are from the asymptotic theory. (The filament radius is $a = R/16$, and the helical pitch is $\lambda = 2.42R$.) For flagella longer than $L/\lambda \sim 100$, the scaled values change slowly, but both the Lighthill and Johnson slender body theory calculations approach the asymptotic value.

where $\kappa = a/\Lambda$ and Λ is the contour length as defined in Fig. 1. The radius of the cross section vanishes at either end of the slender body and is given by $a(s) = a\sqrt{1 - 4s^2/\Lambda^2}$, where $s \in [-\Lambda/2, \Lambda/2]$. The filament radius has an average value of $a\pi/4$; therefore in our Johnson slender body theory calculations we set the filament radius to be $4/\pi$ times the radius used in the experiments and other simulations.

We again use the rectangular rule of integration and the same rotational mapping Eqs. **21**–**24** to numerically evaluate Eq. **31** to obtain

$$\begin{aligned}\mathbf{u}'_n = {} & \frac{1}{8\pi\mu}\left[-\ln\left(\kappa^2 \mathrm{e}\right)\left(\mathbb{I} + \hat{t}'\hat{t}'\right) + 2\left(\mathbb{I} - \hat{t}'\hat{t}'\right)\right] \cdot \mathbf{f}'_n \\ & + \frac{R\Delta\varphi \csc\theta}{8\pi\mu} \sum_{m \neq n} \frac{\mathscr{R}_x(\varphi_m - \varphi_n) + \mathscr{R}_x(-\varphi_n) \cdot \hat{r}_{nm}\hat{r}_{nm} \cdot \mathscr{R}_x(\varphi_m)}{r_{nm}} \cdot \mathbf{f}'_m \\ & - \frac{1}{8\pi\mu} \sum_{m \neq n} \frac{1}{r_{nm}} \left(\mathbb{I} + \hat{t}'\hat{t}'\right) \cdot \mathbf{f}'_n + \mathscr{O}(\Delta\varphi) \end{aligned} \quad [34]$$

$$\begin{aligned}\mathbf{u}'_n = {} & \frac{1}{4\pi\mu}\left[-K\left(\mathbb{I} + \hat{t}'\hat{t}'\right) + \left(\mathbb{I} - \hat{t}'\hat{t}'\right)\right] \cdot \mathbf{f}'_n \\ & + \frac{R\Delta\varphi \csc\theta}{8\pi\mu} \sum_{m \neq n} \frac{\mathscr{R}_x(\varphi_m - \varphi_n) + \mathscr{R}_x(-\varphi_n) \cdot \hat{r}_{nm}\hat{r}_{nm} \cdot \mathscr{R}_x(\varphi_m)}{r_{nm}} \cdot \mathbf{f}'_m \\ & + \mathscr{O}(\Delta\varphi), \end{aligned} \quad [35]$$

where

$$K = \frac{1}{2}\left[\sum_{m \neq n} \frac{1}{r_{nm}} + \ln\left(\kappa^2 \mathrm{e}\right)\right]. \quad [36]$$

This discretized formulation is very similar to the Lighthill version (Eq. **25**), except that the constant $\ln(\delta'/\delta)$ in the D'_n term in Eq. **27** is replaced by $-K$. The net force is solved using the same numerical strategy as used for the Lighthill formulation, giving force, torque, and drag.

Asymptotic Theory for a Long Flagellum

In this section we expand Lighthill's slender body theory to understand the length dependence shown in Fig. 3. Consider a flagellum parameterized by s as in Eq. **16** with a length $L \gg R$ and $L \gg \lambda$. For a sufficiently long helix, end effects are minimal so each segment is essentially the same. Therefore, the force per unit length can be written $\mathbf{f}(s) \approx (f_x, -f_\Omega \sin\varphi, f_\Omega \cos\varphi)$, where f_x is the force per unit length in the x direction and f_Ω is the tangential force per unit length perpendicular to the x direction. The tangential force per unit length has components in the y and z directions, depending on the segment's helical phase $\varphi \equiv ks \cos\theta$, where $k = 2\pi/\lambda$. The associated velocity of the helical filament is $\mathbf{u}(s) = (U, -\Omega R \sin\varphi, \Omega R \cos\varphi)$ so the velocity formulation from Lighthill's slender body theory gives, for the x direction and tangential velocities, respectively,

$$\begin{aligned} U = {} & \frac{(f_x \sin\theta - f_\Omega \cos\theta)\sin\theta}{4\pi\mu} \\ & + \int_{k\delta\cos\theta}^{kL/2} \csc\theta \, \mathrm{d}\varphi \left(\frac{f_x}{4\pi\mu\xi} + \frac{f_\Omega \varphi \sin\varphi \cot\theta + f_x \varphi^2 \cot^2\theta}{4\pi\mu\xi^3}\right) \end{aligned} \quad [37]$$

$$\Omega R = \frac{(-f_x \sin\theta + f_\Omega \cos\theta)\cos\theta}{4\pi\mu} + \int_{k\delta\cos\theta}^{kL/2} \csc\theta \, \mathrm{d}\varphi \left(\frac{f_\Omega \cos\varphi}{4\pi\mu\xi} + \frac{f_\Omega \sin^2\varphi + f_x \varphi \sin\varphi \cot\theta}{4\pi\mu\xi^3} \right), \quad [38]$$

where $\xi(\varphi,\theta) \equiv \sqrt{4\sin^2(\varphi/2) + \varphi^2\cot^2\theta}$, which means $\xi \to \varphi\cot\theta$ as $\varphi \to \infty$ (i.e., $L \gg R, \lambda$).

One can rewrite Eqs. **37** and **38** as

$$\begin{aligned} U &= \frac{[f_x \sin\theta - (\tau_x/R)\cos\theta]\sin\theta}{4\pi\mu} + \int_{\varphi_{\mathrm{ini}}}^{\varphi_{\mathrm{end}}} \csc\theta \, \mathrm{d}\varphi \left[\frac{f_x}{4\pi\mu\xi} + \frac{(\tau_x/R)\varphi\sin\varphi\cot\theta + f_x \varphi^2\cot^2\theta}{4\pi\mu\xi^3} \right] \\ &= \frac{f_x}{4\pi\mu}\left[\sin^2\theta + \int_{\varphi_{\mathrm{ini}}}^{\varphi_{\mathrm{end}}} \csc\theta \, \mathrm{d}\varphi \left(\frac{1}{\xi} + \frac{\varphi^2\cot^2\theta}{\xi^3} \right) \right] + \frac{\tau_x}{4\pi\mu R}\left[-\cos\theta\sin\theta + \int_{\varphi_{\mathrm{ini}}}^{\varphi_{\mathrm{end}}} \csc\theta \, \mathrm{d}\varphi \left(\frac{\varphi\sin\varphi\cot\theta}{\xi^3} \right) \right] \end{aligned} \quad [39]$$

$$\begin{aligned} \Omega &= \frac{[-f_x \sin\theta + (\tau_x/R)\cos\theta]\cos\theta}{4\pi\mu R} + \int_{\varphi_{\mathrm{ini}}}^{\varphi_{\mathrm{end}}} \csc\theta \, \mathrm{d}\varphi \left[\frac{(\tau_x/R)\cos\varphi}{4\pi\mu\xi R} + \frac{(\tau_x/R)\sin^2\varphi + f_x\varphi\sin\varphi\cot\theta}{4\pi\mu\xi^3 R} \right] \\ &= \frac{f_x}{4\pi\mu R}\left[-\sin\theta\cos\theta + \int_{\varphi_{\mathrm{ini}}}^{\varphi_{\mathrm{end}}} \csc\theta \, \mathrm{d}\varphi \left(\frac{\varphi\sin\varphi\cot\theta}{\xi^3} \right) \right] + \frac{\tau_x}{4\pi\mu R^2}\left[\cos^2\theta + \int_{\varphi_{\mathrm{ini}}}^{\varphi_{\mathrm{end}}} \csc\theta \, \mathrm{d}\varphi \left(\frac{\cos\varphi}{\xi} + \frac{\sin^2\varphi}{\xi^3} \right) \right], \end{aligned} \quad [40]$$

where $\tau_x = f_\Omega R$, $\varphi_{\mathrm{ini}} = k\delta\cos\theta$, and $\varphi_{\mathrm{end}} = kL/2$.

It can be shown that the prefactor of f_x in the integrand of Eq. **39** has an asymptotic $O(\ln(\varphi_{\mathrm{end}})) \approx O(\ln(L/R))$ dependence. Elsewhere all other prefactors of f_x and f_Ω in Eqs. **39** and **40** converge for large L. Therefore, the asymptotic form of Eqs. **39** and **40** as $L \to \infty$ is

$$U = a_1 \ln(L/R) f_x + a_2 \tau_x \quad [41]$$

$$\Omega = a_3 f_x + a_4 \tau_x, \quad [42]$$

where

$$a_1 = \lim_{\varphi_{\mathrm{end}}\to\infty} \frac{1}{4\pi\mu\ln(L/R)} \left[\sin^2\theta + \int_{\varphi_{\mathrm{ini}}}^{\varphi_{\mathrm{end}}} \csc\theta \, \mathrm{d}\varphi \left(\frac{1}{\xi} + \frac{\varphi^2\cot^2\theta}{\xi^3} \right) \right] \quad [43]$$

$$a_2 = \lim_{\varphi_{\mathrm{end}}\to\infty} \frac{1}{4\pi\mu R} \left[-\sin\theta\cos\theta + \int_{\varphi_{\mathrm{ini}}}^{\varphi_{\mathrm{end}}} \csc\theta \, \mathrm{d}\varphi \left(\frac{\varphi\sin\varphi\cot\theta}{\xi^3} \right) \right] \quad [44]$$

$$a_3 = a_2 \quad [45]$$

$$a_4 = \lim_{\varphi_{\mathrm{end}}\to\infty} \frac{1}{4\pi\mu R^2} \left[\cos^2\theta + \int_{\varphi_{\mathrm{ini}}}^{\varphi_{\mathrm{end}}} \csc\theta \, \mathrm{d}\varphi \left(\frac{\cos\varphi}{\xi} + \frac{\sin^2\varphi}{\xi^3} \right) \right]. \quad [46]$$

Expressing $\mathscr{F}$ and τ in terms of τ and Ω as $L \to \infty$, we have for the force and torque from Eq. **1**

$$\mathscr{F} = A_{11} U + A_{12}\Omega \quad [47]$$

$$\tau = A_{12} U + A_{22}\Omega, \quad [48]$$

where $A_{11} = (\sec\theta/a_1)L/\ln(L/R)$, $A_{12} = -[a_2\sec\theta/(a_1 a_4)]L/\ln(L/R)$, and $A_{22} = \sec\theta/a_4 L$.

Using Eqs. **47** and **48** and Eqs. **43–46**, one can obtain the following scaling relationships for thrust, torque, and drag in the limit that $L \to \infty$,

$$F = -\frac{a_2\sec\theta}{a_1 a_4}\frac{L}{\ln(L/R)}\Omega \quad [49]$$

$$T = \frac{\sec\theta}{a_4} L\Omega \quad [50]$$

$$D = \frac{\sec\theta}{a_1}\frac{L}{\ln(L/R)} U, \quad [51]$$

as given in Eqs. **4–6**.

We rescale our slender body theory results and plot them in Fig. 9 along with the asymptotic predictions of our theory, showing these scalings are accurate.

ACKNOWLEDGMENTS. We acknowledge Oscar Gonzalez for his advice and for providing a numerical implementation of his boundary integral method. H.P.Z. acknowledges financial support of the National Natural Science Foundation of China through Grant 11104179. H.L.S. acknowledges the support of the Sid W. Richardson Foundation.

1. Gray J, Hancock GJ (1955) The propulsion of sea-urchin spermatozoa. *J Exp Biol* 32: 802–814.
2. Lighthill J (1976) Flagellar hydrodynamics - Neumann, JV Lecture, 1975. *SIAM Rev* 18: 161–230.
3. Friedrich BM, Riedel-Kruse IH, Howard J, Jülicher F (2010) High-precision tracking of sperm swimming fine structure provides strong test of resistive force theory. *J Exp Biol* 213(Pt 8):1226–1234.
4. Sznitman J, Shen X, Sznitman R, Arratia PE (2010) Propulsive force measurements and flow behavior of undulatory swimmers at low Reynolds number. *Phys Fluids* 22:121901.
5. Bayly PV, et al. (2011) Propulsive forces on the flagellum during locomotion of Chlamydomonas reinhardtii. *Biophys J* 100(11):2716–2725.
6. Maladen RD, Ding Y, Umbanhowar PB, Kamor A, Goldman DI (2011) Mechanical models of sandfish locomotion reveal principles of high performance subsurface sand-swimming. *J R Soc Interface* 8(62):1332–1345.

7. Lauga E, DiLuzio WR, Whitesides GM, Stone HA (2006) Swimming in circles: Motion of bacteria near solid boundaries. *Biophys J* 90(2):400–412.
8. Chattopadhyay S, Moldovan R, Yeung C, Wu XL (2006) Swimming efficiency of bacterium Escherichia coli. *Proc Natl Acad Sci USA* 103(37):13712–13717.
9. Chattopadhyay S, Wu XL (2009) The effect of long-range hydrodynamic interaction on the swimming of a single bacterium. *Biophys J* 96(5):2023–2028.
10. Darnton NC, Turner L, Rojevsky S, Berg HC (2007) On torque and tumbling in swimming Escherichia coli. *J Bacteriol* 189(5):1756–1764.
11. Vogel R, Stark H (2010) Force-extension curves of bacterial flagella. *Eur Phys J E Soft Matter* 33(3):259–271.
12. Vogel R, Stark H (2012) Motor-driven bacterial flagella and buckling instabilities. *Eur Phys J E Soft Matter* 35(2):15.
13. Behkam B, Sitti M (2006) Design methodology for biomimetic propulsion of miniature swimming robots. *J Dyn Sys Meas Control* 128:36–43.
14. Abbott JJ, et al. (2009) How should microrobots swim? *Int J Robot Res* 28:1434–1447.
15. Li H, Tan J, Zhang M (2009) Dynamics modeling and analysis of a swimming microrobot for controlled drug delivery. *IEEE Trans Autom Sci Eng* 6:220–227.
16. Ha N, Goo N, Yoon H (2011) Development of a propulsion system for a biomimetic thruster. *Chin Sci Bull* 56:432–438.
17. Johnson RE (1980) An improved slender-body theory for stokes flow. *J Fluid Mech* 99: 411–431.
18. Cortez R, Fauci L, Medovikov A (2005) The method of regularized Stokeslets in three dimensions: Analysis, validation, and application to helical swimming. *Phys Fluids* 17: 031504.
19. Darnton NC, Berg HC (2007) Force-extension measurements on bacterial flagella: Triggering polymorphic transformations. *Biophys J* 92(6):2230–2236.
20. Berg HC (2008) Bacterial flagellar motor. *Curr Biol* 18(16):R689–R691.
21. Koyasu S, Shirakihara Y (1984) Caulobacter crescentus flagellar filament has a right-handed helical form. *J Mol Biol* 173(1):125–130.
22. Scharf B (2002) Real-time imaging of fluorescent flagellar filaments of Rhizobium lupini H13-3: Flagellar rotation and pH-induced polymorphic transitions. *J Bacteriol* 184(21):5979–5986.
23. Macnab RM, Ornston MK (1977) Normal-to-curly flagellar transitions and their role in bacterial tumbling. Stabilization of an alternative quaternary structure by mechanical force. *J Mol Biol* 112(1):1–30.
24. Happel J, Brenner H (1965) *Low Reynolds Number Hydrodynamics* (Prentice Hall, Englewood Cliffs, NJ).
25. Kim S, Karrila J (1991) *Microhydrodynamics: Principles and Selected Applications* (Butterworth-Heinemann, Boston).
26. Jung S, Mareck K, Fauci L, Shelley MJ (2007) Rotational dynamics of a superhelix towed in a Stokes fluid. *Phys Fluids* 19:103105.
27. Yang J, Wolgemuth CW, Huber G (2009) Kinematics of the swimming of Spiroplasma. *Phys Rev Lett* 102(21):218102.
28. Chattopadhyay S (2008) Study of bacterial motility using optical tweezers. PhD thesis (Univ of Pittsburgh, Pittsburgh).
29. Liu B, Powers TR, Breuer KS (2011) Force-free swimming of a model helical flagellum in viscoelastic fluids. *Proc Natl Acad Sci USA* 108(49):19516–19520.
30. Hancock GJ (1953) The self-propulsion of microscopic organisms through liquids. *Proc R Soc Lond Ser A* 217:96–121.
31. Lorentz H (1996) A general theorem on the motion of a fluid with friction and a few results derived from it. *J Eng Math* 30:19–24.
32. Gonzalez O (2009) On stable, complete, and singularity-free boundary integral formulations of exterior stokes flow. *SIAM J Appl Math* 69:933–958.
33. Li J, Gonzalez O (2012) Convergence and conditioning of a Nystom method for Stokes flow in exterior three-dimensional domains. *Adv Comput Math* 1–32.
34. Nguyen H, Ortiz R, Cortez R, Fauci L (2011) The action of waving cylindrical rings in a viscous fluid. *J Fluid Mech* 671:574–586.
35. Hyon Y, Marcos N, Powers TR, Stocker R, Fu HC (2012) The wiggling trajectories of bacteria. *J Fluid Mech* 705:58–76.
36. Lighthill J (1996) Reinterpreting the basic theorem of flagellar hydrodynamics. *J Eng Math* 30:25–34.
37. Lauga E, Powers TR (2009) The hydrodynamics of swimming microorganisms. *Rep Prog Phys* 72:096601.